Imaging Underground Structures Using Broadband Electromagnetic Induction

Alan Witten
School of Geology and Geophysics, University of Oklahoma
Norman, Oklahoma

I.J. Won
Geophex, Inc.
Raliegh, North Carolina

Stephen Norton
Energy Division, Oak Ridge Nation Laboratory
Oak Ridge, Tennessee

ABSTRACT

Broadband electromagnetic induction is a promising technique for the detection and location of underground structures. Along with being simple to use and allowing rapid data acquisition, underground structures can be detected by this method either because the large volume of air necessary for human occupancy will be manifested as an electrical conductivity low relative to the host formation or because there could exist a large metallic mass associated with either structural support or the mission of the facility that would constitute a relative conductivity high. The use of broadband information literally offers an additional dimension, that being depth, to the level of information that can be gleaned from acquired data since, by varying the operating frequency, the probing depth changes. A three-dimensional tomographic imaging algorithm is applied to broadband data acquired at two underground structure sites to reconstruct the relative spatial variations in electrical conductivity. A pair of parallel subway tunnels exist at one site and a cloud chamber at the other. At both sites, quite good images of the structures were obtained and the structures appeared as relative conductivity lows.

Introduction

Under ideal conditions, almost any geophysical tool can be used to detect and located subsurface structures suitable for human occupancy. In practice, however, the choice of geophysical method will be dictated by the anticipated size and depth of the underground structure as well as site conditions including the mechanical and electrical properties of the host geology, whether data can be acquired directly over the underground structure, and the presence of surface or near surface cultural features.

Beyond the above-cited issues that may influence the choice of geophysical methods, there may be operational constraints that must additionally be considered. There are a number of scenarios under which site access time is severely limited and data must be acquired by operators with no geophysical training. In such cases, electromagnetic induction (EMI) is a strong candidate since EMI tools are relatively simple to operate and data can be acquired quite rapidly. Broadband EMI is particularly attractive since, by its nature, it offers information about target depth with no additional complications in data acquisition.

It has been shown (Won, 1980) that a pseudo cross-sectional image can be obtained from broadband EMI measurements made at intervals along a line. By displaying this data as a vertical slice having a depth axis inversely proportional to the square root of the acquisition frequency, a crude form of an image of spatial variations in electrical conductivity within the cross-section is produced. This technique is referred to as frequency sounding. In a more recent development, Witten, Won, and Norton (1997) established that frequency sounding produced an out-of-focus image of conductivity anomalies and presented a generalized form of diffraction tomography (Devaney, 1984) whereby focused images may be reconstructed.

In this paper, the general concept of frequency sounding is discussed and a three-dimensional broadband EMI imaging algorithm is summarized. This algorithm is applied to broadband EMI data acquired at two sites known to contain underground structures.

EMI Imaging Concepts

The use of EMI in geophysics exploits the fact that a current will be induced in an electrically conductive anomaly, when immersed in a time-varying electromagnetic field. In turn, the current induced in conductive anomalies will induce a (secondary) time-varying electromagnetic field. Thus, EMI measurements can be used to detect and locate subsurface, electrically conductive features by creating a time-varying field

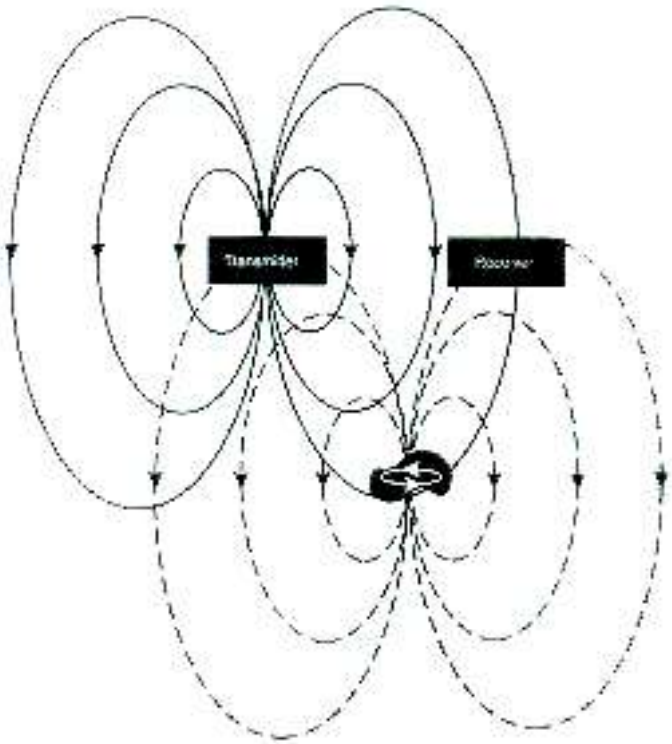

Figure 1. Illustration showing transmitting coil producing a primary field (solid contours). This field induces a current in a conductor (black mass) that, in turn, produces a secondary field (dashed contours) detected by the receiving coil.

using a transmitting coil and measuring the induced secondary field with a receiving coil (fig. 1). Because rock and soil are somewhat conductive and will produce a secondary field when exposed to a primary field, EMI can also be used to detect anomalous features that are more resistive than the background.

In general, there are two methods by which depth information can be extracted from EMI measurements. These are geometrical soundings and broadband soundings. In geometrical soundings, measurements are made at a fixed frequency for a range of separation distances between the transmitting and receiving coils while, for broadband soundings, decreasing the frequency is associating with deeper probing. This study deals only with broadband soundings. In a conducting medium, electromagnetic waves will both oscillate and decay with distance from the source and both the wavenumber and the decay rate are proportional to the frequency. Figure 2 depicts two conducting targets at two different depths below a transmitting coil generating a primary field with conductor 1 being the shallower target. Since this primary field decays with distance, conductor 1 is immersed in a stronger field than conductor 2 and, hence, a stronger current and, consequently, a stronger secondary field is induced in this conductor. Furthermore, there will be greater decay of the secondary field from conductor 2 since it is farther away from a receiving coil taken to be located alongside the transmitting coil. The receiving coil will measure a secondary field that is a composite of the response of both conductors with this measured response being a depth-integrated function of the conductivity inversely weighted by the depth.

Figure 3 is a sequence of illustrations designed to show how broadband soundings can be used to quantify target depth. In fig. 3a, the driving frequency is sufficiently high that the primary field decays to a negligibly small value before it reaches the depth of the conductive anomaly. Decreasing the frequency (fig. 3b), decreases the rate of decay of the primary field such that a measurable response to the anomaly is produced at the receiver coil. When the frequency is so low that the primary field penetrated to a depth much greater than the conducting target (fig. 3c), the anomaly is only weakly manifested in the measured secondary because, as noted above, this field is depth average and the anomaly occupies only a small portion of the penetration depth. Thus, decreasing the frequency below that shown in fig. 3b will produce a gradual decay in the measured secondary field. Figure 3d shows an idealized magnitude of the measured secondary field as a function of frequency illustrating the broadband sounding concept.

A measure of the penetration depth of a primary field is the skin depth, δ, defined to be

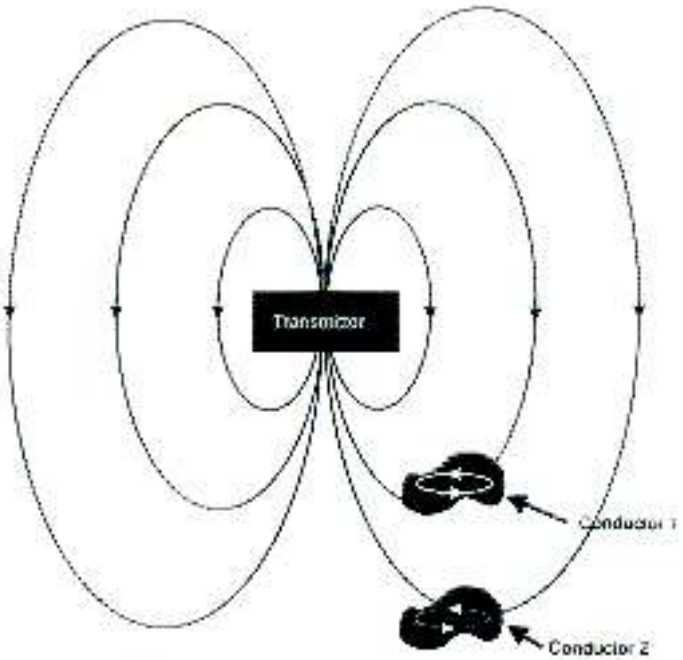

Figure 2. Illustration showing two conductors at different depths below a transmitting coil. Since conductor 2 is further away from the transmitting coil than conductor 1, a weaker current (indicated by the narrower white line depicting the current loop) is induced in this feature.

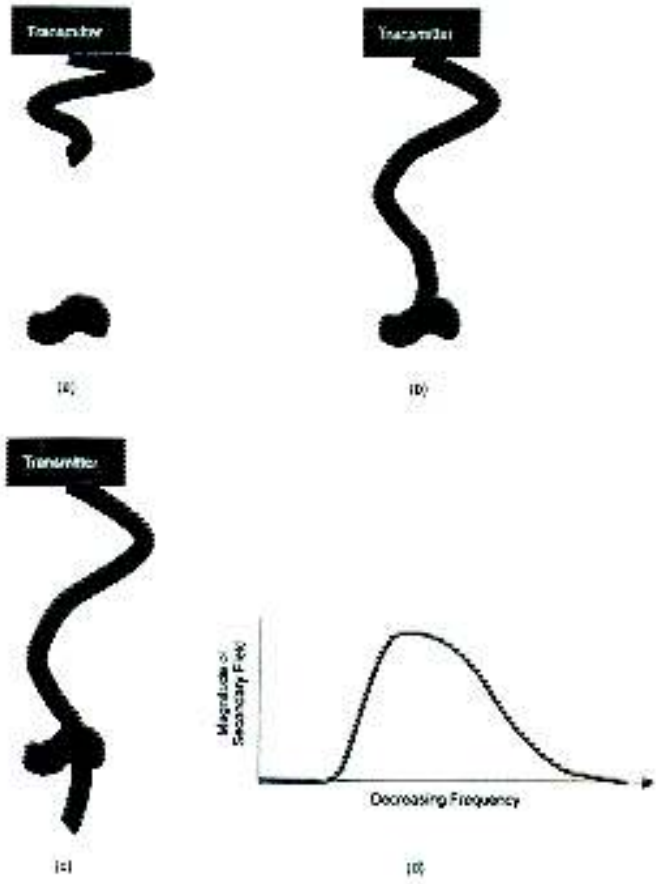

Figure 3. Illustration showing the oscillation and decay of a time-varying electromagnetic field and a conductor below the transmitting coil for a) a high frequency, b) a moderate frequency, and c) a low frequency. The variation in secondary field strength as a function of frequency is shown in d).

$$\delta = \frac{\sqrt{2}}{\sqrt{\omega \mu_0 \sigma_0}} \qquad (1)$$

where ω is the frequency, μ_0 is the background magnetic susceptibility, and σ_0 is the background conductivity. Won (1980) demonstrated that broadband soundings such as that shown in fig. 3d will peak at a skin depth corresponding to the target depth. Figure 4 is simulated data for measurements made by traversing the ground surface with a co-located transmitting/receiving coil pair making measurements every meter for a range of frequencies corresponding to uniformly-spaced skin depths between 1 and 32 meters. The target assumed here is a rectangular conductor dimensioned 12 horizontally by 8 vertically centered at (15.5,-16.5). This figure displays the in-phase component of the output voltage from the secondary coil as gray levels as a function of measurement location and skin depth. It is clear that the data, so displayed, is an out-of-focus image of the rectangular target with the target appearing at a skin depth near the target depth. The phase changes appearing in the pseudo-image are a result of the fact that both the primary and secondary field are spatially oscillatory. The next section will describe tomographic imaging concepts whereby out-of-focus images, such as that shown in fig. 4 can be sharpened and the phase changes removed.

Broadband EMI Imaging

One means to describe the EMI imaging concept is through the related problem of imaging using seismic reflection and specifically migration. For a co-located seismic source and receiver deployed over the plane $\mathbf{r} = (x,y)$, the spatially and temporally Fourier transformed received signal

$$\tilde{u}(\kappa,\omega) = \int dt\, e^{i\omega t} \int d\mathbf{r}\, e^{-i\kappa\cdot\mathbf{r}}\, u(\mathbf{r},t) \qquad (2)$$

is related to the three-dimensional reflectivity by

$$R(x,y,z) = \frac{1}{8\pi^3} \int d\omega \int d\kappa\, \exp\{i(\sqrt{4k^2-\kappa^2}\,z + \kappa\cdot r)\}\, \tilde{u}(\kappa,\omega) \qquad (3)$$

(Cheng and Coen, 1984), where $k = \omega/c_0$, c_0 is the background wave speed and κ is the magnitude of the two-dimensional vector κ. Spatial variations in reflectivity are recon-

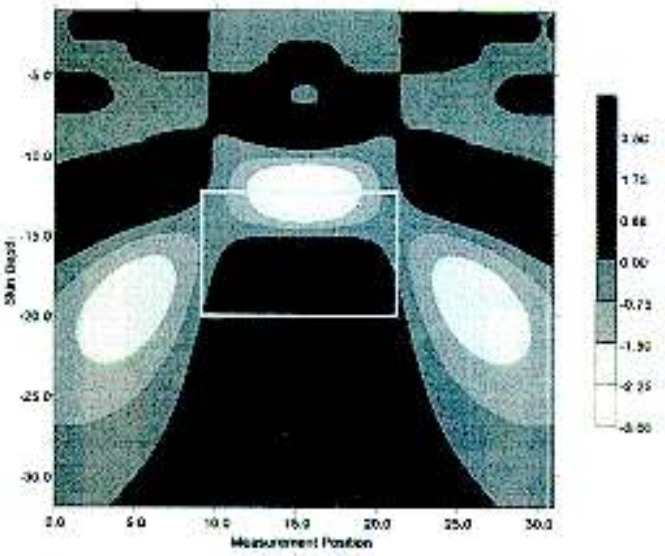

Figure 4. Simulated broadband data for measurements made at uniformly spaced points on the ground surface over the top of 12 by 8 m rectangular conductor buried at an assumed depth of -16.5 m. The horizontal axis is the measurement location and the vertical axis is skin depth. In this form, the data appears as an out-of-focus image. The gray rectangular outline displays the size, shape, and depth of the target.

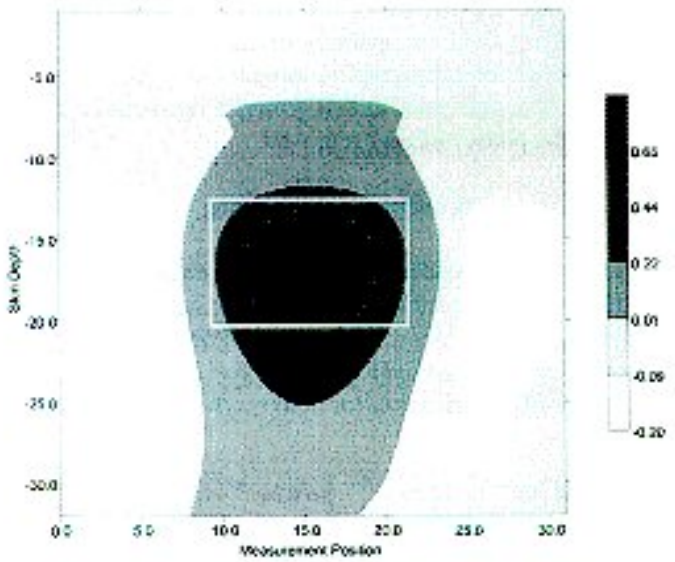

Figure 5. Vertical cross-sectional image reconstructed from the simulated broadband data shown in Fig. 4. The outline of the actual assumed target is outlined in gray.

structed in Eq. (3) by backpropagating (migrating) the data u downward to some plane $z < 0$ and evaluating this data at time zero. In a similar approach within the framework of diffraction tomography, the spatial variations of the object function, $O(x,y,z) = 1 - c_0^2/c^2(x,y,z)$, are reconstructed by

$$O(x,y,z) = \frac{1}{8\pi^3}\int d\omega \int d\kappa\, H(\kappa,\omega) \exp\{i(\sqrt{4k^2-\kappa^2}\,z + \kappa\cdot r)\}\,\tilde{u}(\kappa,\omega) \qquad (4)$$

where $c(x,y,z)$ are the spatial variations in wave speed about c_0 and H is measurement geometry-specific filter function. The three-dimensional spatial Fourier transform of Eq. (4) is

$$\tilde{O}(\kappa,\sqrt{4k^2-\kappa^2}) = H(\kappa,\omega)\,\tilde{u}(\kappa,\omega) \qquad (5)$$

and it is clear that the object function can be reconstructed by applying an invers Fourier transform to Eq. (5). Equations relating the spatial Fourier transform of data to the spatial Fourier transform of the object function, such as Eq. (5), are known as generalized projection slice theorems (Devaney, 1984).

A generalized projection slice theorem for broadband EMI imaging (Witten, Won, and Norton, 1997) relating the spatially Fourier transformed output voltage from the receiving coil, $V(x,y)$, to an integral transform of the object function, is

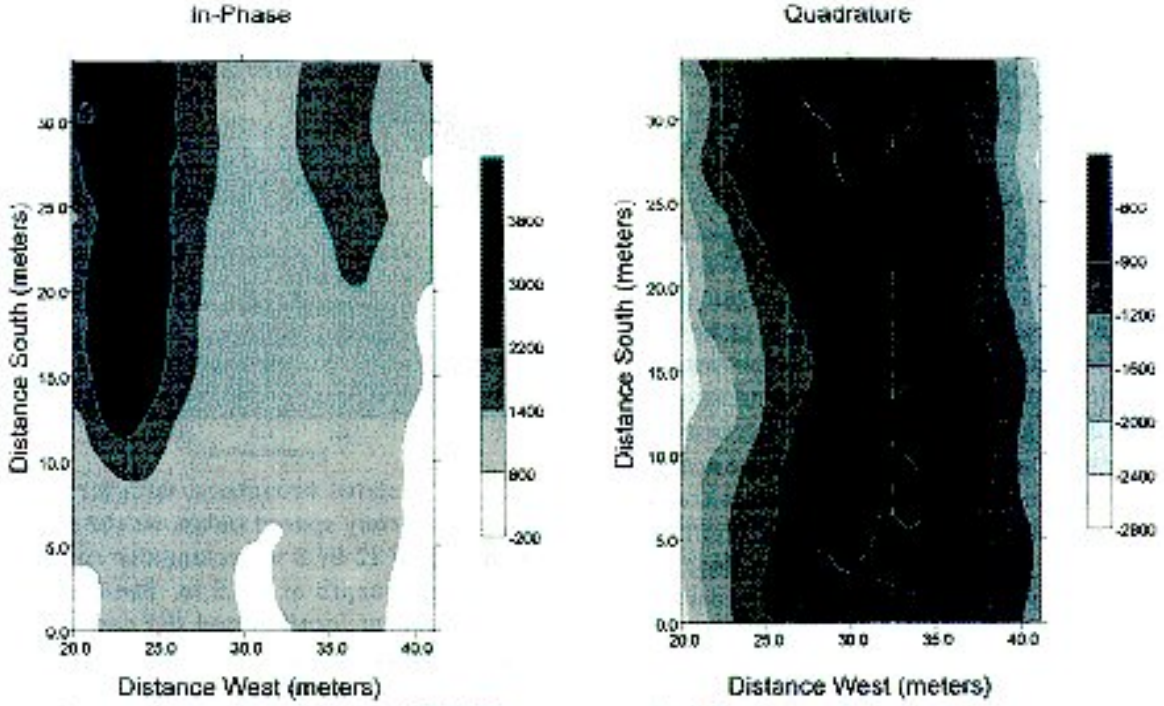

Figure 6. In-phase and Quadrature data at 9810 Hz as measured at the Anacostia tunnel site.

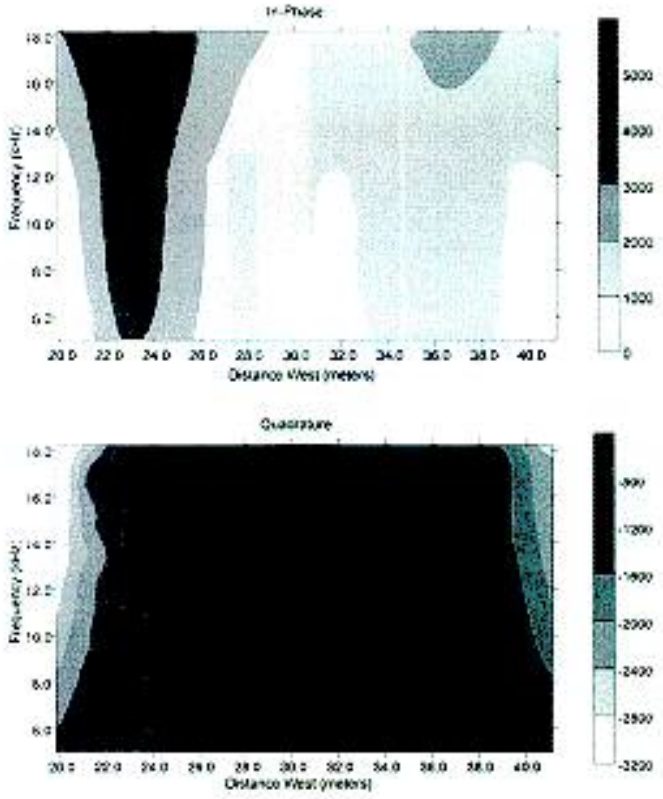

Figure 7. Pseudo image of the Anacostia data presented as measurement location along a line at 21 m north as a function of frequency (the vertical axis).

$$\bar{O}(\kappa, \sqrt{(32i\pi^2/\delta^2) - \kappa^2}) = H(\kappa,\omega)\ \bar{V}(\kappa,\omega), \tag{6}$$

where $O(x,y,z) = (\sigma(x,y,z)/\sigma_0) - 1$ and $\sigma(x,y,z)$ are the spatial variations in conductivity relative to a background σ_0. The most important difference between this relationship and that for wave-based imaging, Eq. (5), is that the vertical component of the wave vector in Eq. (5) is real while that for EMI imaging, Eq. (6), is complex and cannot be completely inverted by Fourier transform. The inversion of Eq. (6) can be expressed in the form

$$O(x,y,z) = \frac{1}{2\pi^2} \int d\kappa\ e^{i\kappa \cdot r}\ \bar{O}(\kappa,z), \tag{7}$$

where the object function is reconstructed by performing an inverse two-dimensional (horizontal) Fourier transform of $\bar{O}$ and $\bar{O}$ is the inverse of the integral transform

$$\bar{O}(\kappa, \sqrt{(32i\pi^2/\delta^2) - \kappa^2}) = \int dz\ H(\kappa,\omega)\ \exp\{-i\sqrt{(32i\pi^2/\delta^2) - \kappa^2}\, z\}\ \bar{V}(\kappa,\omega). \tag{8}$$

Equation (8) is a mapping from depth into skin depth and consequently its inverse is a mapping from skin into depth. Since this integral transform is characterized by a complex wave number, it cannot be inverted by Fourier transform. In the algorithm developed here, Eq. (8) is inverted by matrix inversion, however, this procedure is ill-conditioned necessitating the use of a regularization procedure.

Figure 5 is an image resulting form the application of this reconstruction procedure to the broadband data presented in fig. 4. It is clear that this imaging algorithm serves to focus the pseudo-image and removes phase changes evident in fig. 4.

Case Studies

The broadband EMI imaging algorithm has been applied to data acquired at two underground structure sites. At both sites, data were acquired with the GEM-2 sensor (Won, Keiswitter, Fields, and Sutton, 1996). This broadband tool consists of a transmitting and receiving coil located at opposite ends of a boom that is approximately two meters long. A third coil, the "bucking" coil, is used to nullify the primary field at the receiving coil so that this coil responds only to the much weaker secondary field. The GEM-2 can operate at frequencies up to 22kHz.

There are two notable differences between GEM-2's operation and configuration and assumptions made in the imaging algorithm. First, the imaging algorithm assumes that the transmitting and receiving coils are co-located while these coils are separated in the GEM-2. This inconsistency can potentially produce errors in the reconstructed images where

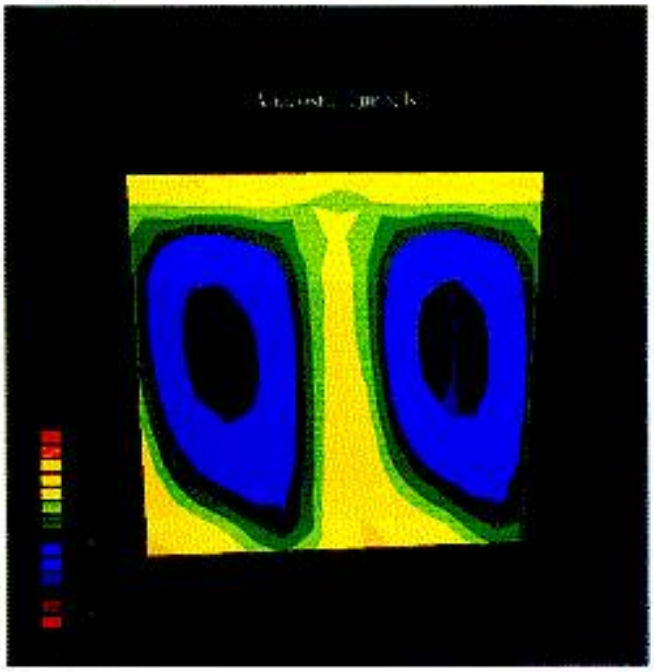

Figure 8: Three-dimensional rendering of the reconstructed image of the subway tunnels at the Anacostia site.

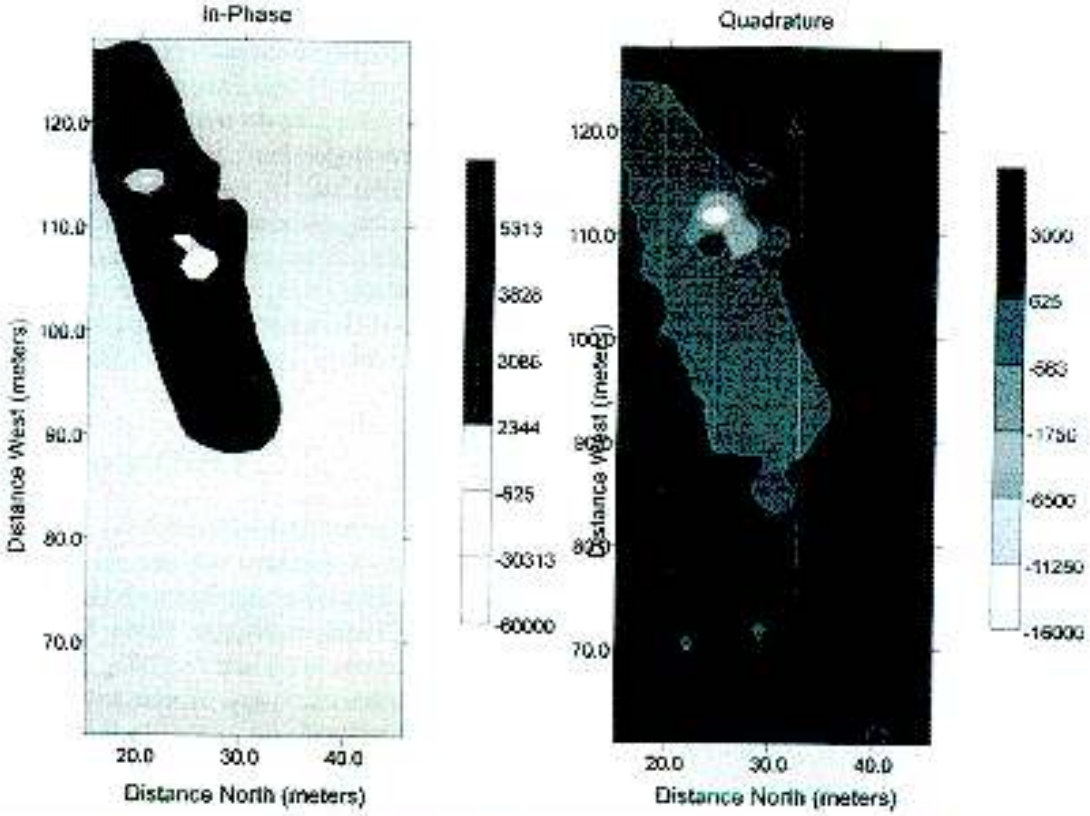

Figure 9: In-phase and Quadrature data at 9270 Hz as measured at the cloud chamber site.

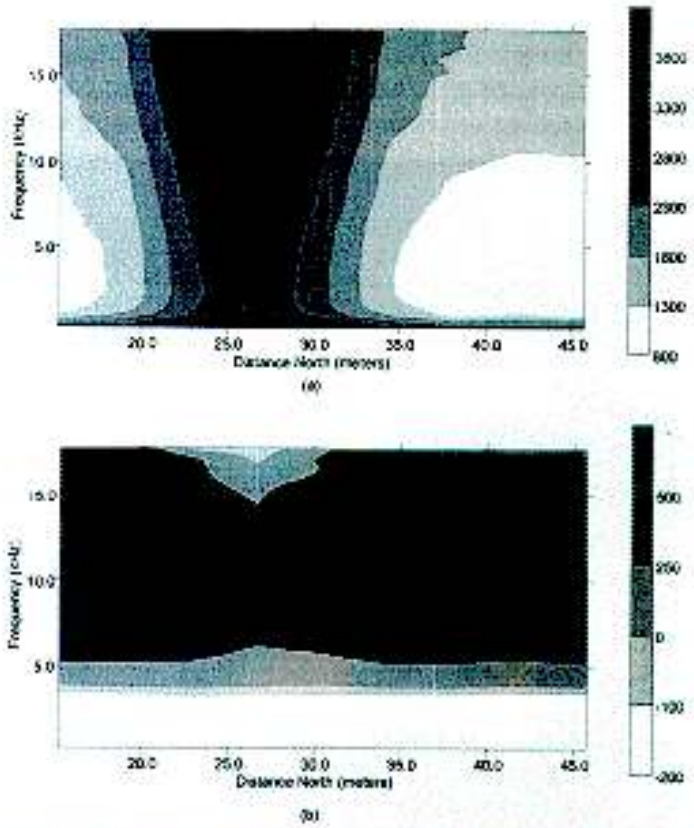

Figure 10: Pseudo image of the cloud chamber data presented as measurement location along a line at 99 m west as a function of frequency (the vertical axis).

the magnitude of such errors will depend on the target depth, the coil separation, and frequencies used in the reconstruction. For the parameters appropriate to the case studies presented here, errors associated with the coil separation can be shown to be negligible. The imaging algorithm described in the previous section is based on output voltage at the receiving coil associated with secondary field. The instrument-specific parameters that influence this voltage are the diameter, number of turns, and orientation of both the transmitting and receiving coils as well as the amperage and frequency applied to the transmitting coil. These parameters appear explicitly in the filter H appearing in Eq. (8). The GEM-2 output is the ratio of the secondary to primary field at the receiving coil in parts per million which is linearly related to receiving coil output voltage. Because of the difference between the actual output from the GEM-2 and that assumed in the imaging algorithm, absolute conductivities cannot be reconstructed, however, reconstructed values of the object function are expected to be correct in a relative sense.

The Anacostia Site

The Anacostia site is vacant lot about 152 m from the Washington, D.C. Anacostia metro station. GEM-2 broadband EMI data were acquired over an area approximately 44 m by 30 m. Part of this area was marshy with standing water varying in depth up to about 0.35 m. The target of interest at this site is a pair of parallel subway tunnels having a center-to-center

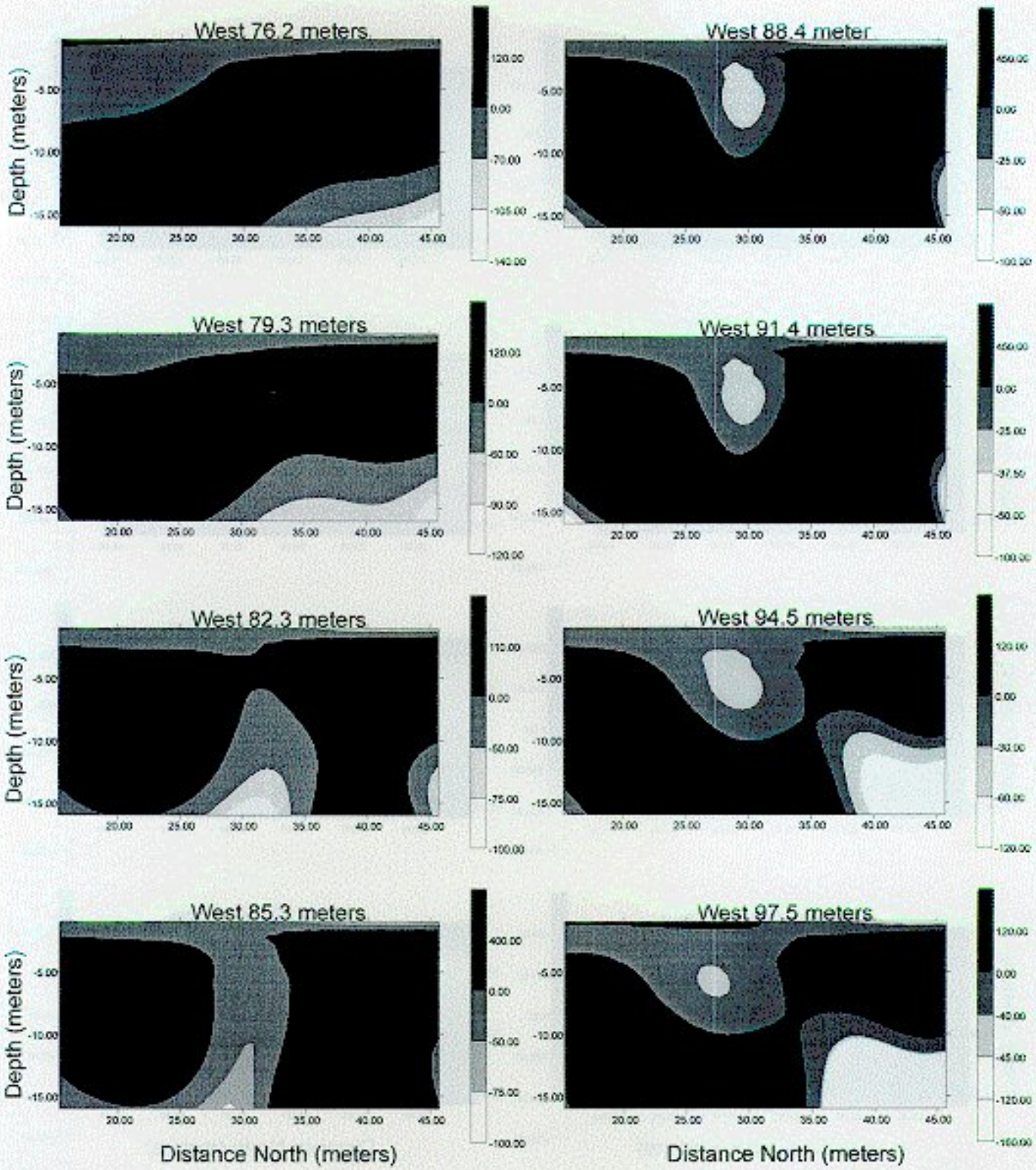

Figure 11a. Three-dimensional image of the cloud chamber displayed as 16 uniformly spaced vertical cross-sections at 76.2 through 97.5 m west.

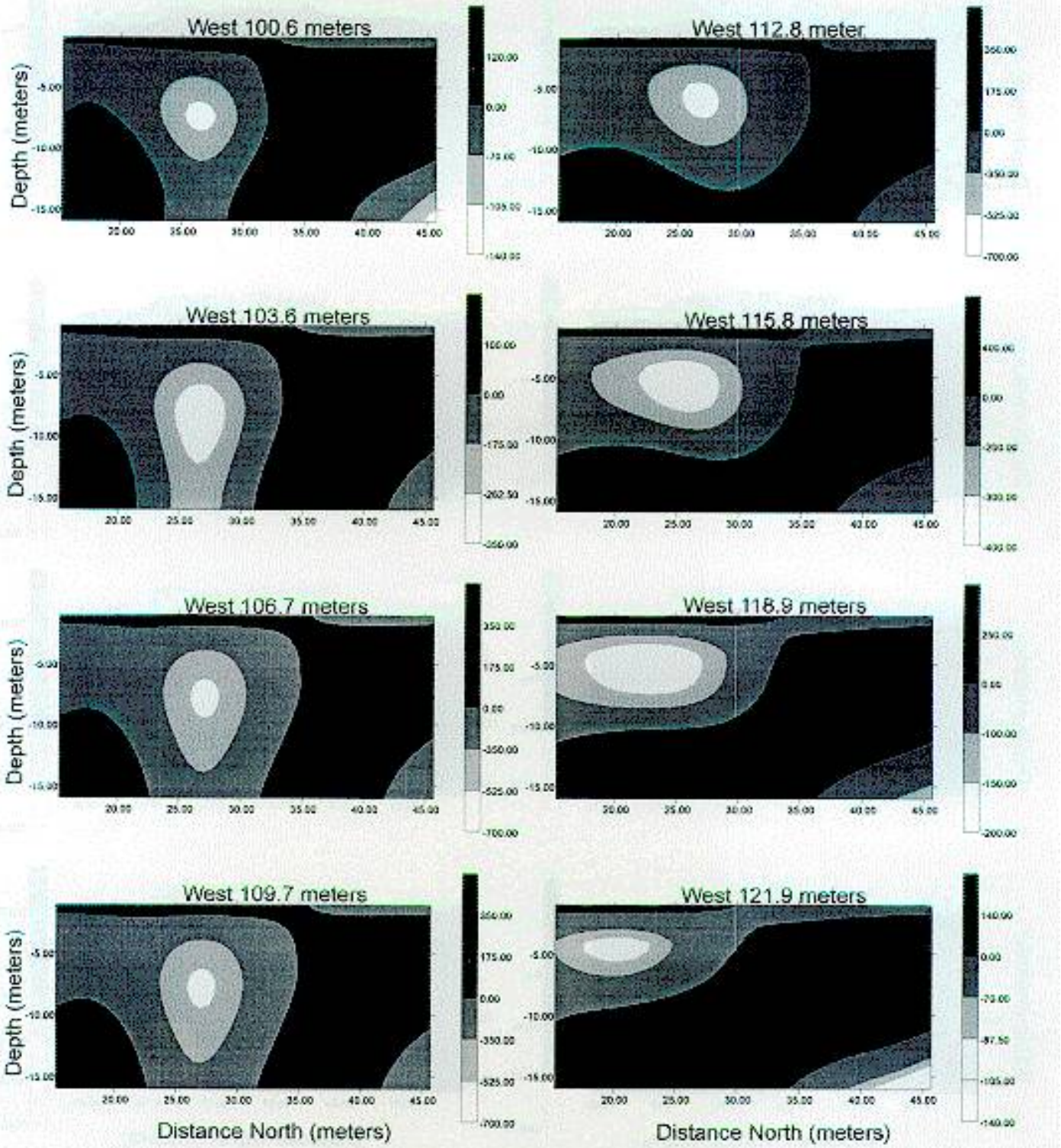

Figure 11b. Three-dimensional image of the cloud chamber displayed as 16 uniformly spaced vertical cross-sections at 100.6 through 121.9 m west.

separation of about 12 m. The axes of these tunnels are oriented in a north-south direction. Each tunnel is approximately 4.5 m in diameter and the tunnel ceilings are believed to be 10 to 13 m below the ground surface. GEM-2 measurements were made at 28 points spaced at 1.524 m in the east-west direction and at 11 points spaced at 3.048 m in the north-south direction. At every measurement point data were acquired with a vertical coil axes orientation for 23 discrete frequencies ranging from 5010 Hz to 18210 Hz in 600 Hz increments.

Figure 6 shows the in-phase and quadrature measurements at 9810 Hz from the Anacostia site. Over the northern half of the survey area both tunnels are manifested in the in-phase data with the western tunnel producing a stronger anomaly. In the southern half, however, there is little evidence of the either tunnel presumably because of an increase in tunnel depth or a change in background conductivity. The existence of the tunnel pair is evident over the entire north-south extent of the quadrature data, however, in this case the individual tunnels are indistinct. This general pattern in typical of data acquired at all frequencies. Figure 7 is a pseudo cross-sectional image of the in-phase component of a slice occurring at 21 m north similar to the synthetic data shown in fig. 4. Here the vertical axis is decreasing frequency and it is expected that there should a localized anomaly occurring at a frequency associated with a skin depth, Eq. (1), corresponding to the target depth. A localized anomaly does occur for the eastern tunnel at a frequency of about 17 kHz, however, there is no relative high or low for the western tunnel.

Figure 8 is a three-dimensional rendering of the image reconstructed from the GEM-2 data using the imaging algorithm described in the previous section. Sixteen frequencies ranging from 5010 Hz to 14010 Hz were used to compute the object function at 16 depths ranging from 1 to 23.5 m and an assumed background conductivity of 0.1 Siemen/m. In this image, rendered with EarthVision software[1], the lowest values of object function (those associated with the lowest relative conductivity) were removed to give the subway tunnels a hollow appearance. In this image, the tunnels have the correct separation and horizontal diameter. The tunnels are vertically elongated in the image resulting in a vertical dimension that is slightly too large and a depth to tunnel ceilings that is slightly too small, however, the depth to the tunnel centers is approximately correct.

The Cloud Chamber Site

The cloud chamber site exists on the Department of Energy's Nevada Test Site in Nye County, Nevada. As its name implies, the target of interest at this site is cloud chamber original built to measure certain properties of ionized particles. The cloud chamber has not been used since 1968. This underground structure is shaped like a quonset hut, 42.7 m long, 9.75 m wide at its base, with a maximum height of 4.9 m. The depth to the roof of the cloud chamber is about 5 m.

GEM-2 measurements were over a rectangular region approximately 30 m north-south by 67 m east-west. Data were acquired at uniformly spaced intervals of 1.524 m in both directions. Thirty frequencies ranging from 270 Hz to 17670 Hz in intervals of 600 Hz were used for both vertical and horizontal coil axis orientation. Figure 9 shows the acquired in-phase and quadrature data at 9270 Hz for the vertical coil axis orientation. The cloud chamber is clearly manifested in both components of this data as the rectangular anomaly extending diagonally from about 30 m north, 100 m west to about 20 m north, 120 m west. Smaller anomalous features evident in the data are associated with vents and an access shaft. The data presented in this figure is typically of the entire frequency range. Figure 10 displays the entire acquired vertical coil axis frequency band along a line at 99 m west as a pseudo cross-sectional image. As in fig. 7, the vertical axis is decreasing frequency (increasing skin depth). The lateral location of the cloud chamber is clearly resolved, however, the highest frequencies used were too low to allow the resolution of the top of this feature.

A subset of the broadband, vertical coil axis EMI data was input to the above-described imaging algorithm. Here, 16 uniformly-spaced frequencies ranging from 8670 Hz to 17670 Hz were used. The full range of measurement points in the north-south direction were used but data in the east-west direction were limited to a sub-region extending from 76 m to 122 m west at 3.048 m intervals. Figure 11 displays the three-dimensional image reconstructed at a background conductivity of 0.004 Siemen/m as 16 parallel vertical cross-sections. Although the contrast scale changes from cross-section to cross-section, the cloud chamber appears in these images as a relative conductivity low in approximately the proper horizontal location and over the correct approximate depth interval. The width of the cloud chamber is about 50% too small in many of the cross-sections.

Conclusions

Underground structures at two sites have been imaged with broadband EMI data. Based on this experience and in the absence of any horizontally-broad, near-surface high conductivity anomalies, it is possible to image other underground structures of similar size and depth. Furthermore, it is anticipated that deeper underground structures can similarly be imaged since the fundamental limiting parameter in EMI imaging is the penetration depth. At least with the GEM-2 EMI tool, it is possible to acquire data down to the DC level suggesting that great penetration depths can be achieved allowing the imaging of much deeper structures, albeit with an attendant loss of spatial resolution.

The ability to image shallow targets within the frequency range considered here is somewhat speculative. This is because the lack of high frequency information will, in turn, limit mapping between target depth and skin depth to the point

where the inversion of Eq. (8) is no longer robust. Although the bandwidth used here yielded skins depths that were, at best, no less than the target, it is unclear at this time how much shallower the imaging algorithm can be stressed.

References

Cheng, G. and Coen, S., 1984, The relationship between Born inversion and migration for common-midpoint stacked data, Geophysics, **49**, 2117-2131.

Devaney, A.J., 1984, Geophysical diffraction tomography, IEEE Trans. Geosci. And Remote Sensing, **GE-22**, 3-13.

Witten, A.J., Won, I.J., and Norton, S.J., 1997, Subsurface imaging with broadband electromagnetic induction, submitted to Inverse Problems.

Won, I.J., 1980, A wide-band electromagnetic induction method: some theoretical and experimental results, Geophysics, **45**, 928-940.

Won, I.J., Keiswetter, D.A., Fields, G.R.A., and Sutton, L.C., 1996, A new multifrequency electromagnetic sensor, J. Env. and Eng. Geophysics, 1, 129-137.

[1] EarthVision is a registered trademark of Dynamic Graphic, Inc.